Journal of Solid State Chemistry 184 (2011) 1153–1158

Contents lists available at ScienceDirect

Journal of Solid State Chemistry

journal homepage: www.elsevier.com/locate/jssc

Nanosized copper ferrite materials: Mechanochemical synthesis and characterization

Elina Manova [a], Tanya Tsoncheva [b,*], Daniela Paneva [a], Margarita Popova [b], Nikolay Velinov [a], Boris Kunev [a], Krassimir Tenchev [a], Ivan Mitov [a]

[a] Institute of Catalysis, Bulgarian Academy of Sciences, Acad. G. Bonchev Str., Bl. 11, 1113 Sofia, Bulgaria
[b] Institute of Organic Chemistry with Centre of Phytochemistry, Bulgarian Academy of Sciences, Acad. G. Bonchev Str., Bl. 9, 1113 Sofia, Bulgaria

ARTICLE INFO

Article history:
Received 23 November 2010
Received in revised form
16 March 2011
Accepted 18 March 2011
Available online 22 March 2011

Keywords:
Mechanochemical synthesis
Copper ferrite
Mössbauer spectroscopy
Methanol decomposition
Toluene oxidation

ABSTRACT

Nanodimensional powders of cubic copper ferrite are synthesized by two-steps procedure of co-precipitation of copper and iron hydroxide carbonates, followed by mechanochemical treatment. X-ray powder diffraction, Mössbauer spectroscopy and temperature-programmed reduction are used for the characterization of the obtained materials. Their catalytic behavior is tested in methanol decomposition to hydrogen and CO and total oxidation of toluene. Formation of nanosized ferrite material is registered even after one hour of milling time. It is established that the prolonging of treatment procedure decreases the dispersion of the obtained product with the appearance of Fe_2O_3. It is demonstrated that the catalytic behavior of the samples depends not only on their initial phase composition, but on the concomitant ferrite phase transformations by the influence of the reaction medium.

1. Introduction

Transition metal spinel oxides are technologically important as magnetic materials, semiconductors, pigments and as effective catalysts for number of industrial processes, such as aluminum production [1–4], oxidative dehydrogenation of butane to butadiene, two step thermochemical methane reforming [5], hydrodesulphurization of petroleum, photo-catalytic reactions [6], CO oxidation [7], treatment of automotive exhausted gases [8], hydrogen production by steam reforming of DME [9–11], etc. Copper ferrite is an inverse ferromagnetic spinel, which could be described as a cubic closed packed arrangement of oxygen ions with Cu^{2+} and Fe^{3+} cations in tetrahedral (A) and octahedral (B) coordination. The cations distribution in this structure can be represented by $(Cu_xFe_{1-x})_A(Cu_{1-x}Fe_{1+x})_BO_4$, where x is the inversion parameter and $x=0$ and 1 stands for the inverse and normal cases, respectively [12,13]. The crystal symmetry and the properties of these ferrites are highly sensitive to the cations distribution, which in turn depends on the method of preparation. It was established that depending on the preparation method, $CuFe_2O_4$ can crystallize either in tetragonal or cubic symmetry [14,15]. Although the stable low temperature ferrite phase is tetragonal, a deficit of Cu^{2+} cations in the B-sublattice leads to the absence of cooperative Jan-Teller distortion and transformation of crystal phase to cubic one [1,13–19]. Nedkov et al. [19] considered the formation of cubic structure of $CuFe_2O_4$ at temperatures bellow 600 K and tetragonal one above 700 K. Jiang et al. [12] demonstrated the predominant formation of $CuFe_2O_4$ with tetragonal unit cell symmetry if the sample is slowly cooled from high temperatures.

Nanosized spinel ferrites show unusual properties in comparison with their bulk analogs and receive enormous attention during last decade because of their potential applications [20–22]. They can be obtained by variety of methods such as solid state reaction [23,24], sol–gel [25], co-precipitation [23,25–27] and combustion synthesis [28]. The use of ball-milling [1,12,13] is alternative synthesis route with the preparation of material with particles in nanometer scale, with high vacancy densities and variations in the site population.

The aim of the present work is to investigate the possibility of $CuFe_2O_4$ nanodimensional powders synthesizing by co-precipitation of the corresponding hydroxide carbonate followed by mechanochemical treatment. The relationship between synthesis parameters, phase composition, structural and catalytic properties of the obtained materials is studied. Methanol decomposition to CO and hydrogen as well as total oxidation of toluene were used as test reactions in order to follow the effect of the reduction and oxidation reaction atmosphere, respectively, on the phase transformations of the obtained spinel materials.

2. Experimental

2.1. Materials

The synthesis of copper ferrites was performed by two step procedure, including (1) co-precipitation and (2) mechanical milling of the co-precipitation precursors as it was described in

* Corresponding author.
E-mail address: tsoncheva@orgchm.bas.bg (T. Tsoncheva).

0022-4596/$ - see front matter © 2011 Elsevier Inc. All rights reserved.
doi:10.1016/j.jssc.2011.03.035

[29]. Co-precipitated hydroxide carbonates, which were used as precursors were prepared from aqueous solutiuon of $Fe(NO_3)_3 \cdot 9H_2O$ and $Cu(NO_3)_2 \cdot 3H_2O$ by dropwise addition of 1 M sodium carbonate up to pH 9 at continuous stirring. After washing (until the absence of nitrates) and drying at RT, brown substances are formed, denoted as CuFe(HC). The as-obtained precursor powders were milled using a Fritsch Planetary miller in a hardened steel vial together with grinding balls having different diameters (from 3 to 10 mm). The precursors were mechanically milled for 1, 2, 3 and 5h. Samples were denoted as CuFe(x), where x corresponds to the duration of milling treatment in hours.

2.2. Methods of investigation

The powder XRD patterns were recorded by use of a TUR M62 diffractometer with Co $K\alpha$ radiation. The observed patterns were cross-matched with those in the JCPDS database. The room temperature (RT) and liquid nitrogen temperature (LNT) Mössbauer spectra were obtained with a Wissel (Wissenschaftliche Elektronik GmbH, Germany) electromechanical spectrometer working in a constant acceleration mode. A ^{57}Co/Cr (activity $\cong$10 mCi) source and a α-Fe standard were used. The experimentally obtained spectra were fitted to mathematical processing according to the least squares method. The parameters of hyperfine interaction such as isomer shift (δ), quadrupole splitting (Δ), effective internal magnetic field (B), line widths (Γ_{exp}) and relative weight (G) of the partial components in the spectra were determined. Temperature-programmed reduction (TPR) of the samples was carried out in the measurement cell of a differential scanning calorimeter (DSC-111, SETARAM) directly connected to a gas chromatograph (GC). Measurements were made in the 300–973 K range at 10 K/min heating rate in a flow of Ar:H_2=9:1, the total flow rate being 20 ml/min. A cooling trap between DSC and GC removes the water obtained during the reduction.

Methanol decomposition experiments were carried out in a flow reactor using argon as a carrier gas, at methanol partial pressure of 1.57 kPa and WHSV-1.5 h^{-1}. On-line gas chromatographic analysis were performed on HP 5890 on PLOT Q column, with simultaneous using of detector of thermo conductivity and flame ionization detector and an absolute calibration method. Toluene oxidation was studied at atmospheric pressure using a fixed-bed flow reactor, air as carrier gas and 30 mg sample (particle size 0.2–0.8 mm) diluted with 60 mg glass beads of the same diameter previously checked to be inactive. The air stream passed through a saturator filled with toluene and equilibrated at 273 K ($p_{toluene}$=0.9 kPa). The activity was determined in the temperature interval of 623–723 K at WHSV-1.2 h^{-1}. On-line analysis of the reaction products were performed using HP-GC with a 25 m PLOT Q capillary column.

3. Results and discussion

3.1. Physicochemical characterization

XRD patterns of the obtained pair copper and iron materials are presented in Fig. 1. Before the milling procedure only broad reflections of hydroxide carbonate precursor, CuFe(HC), could be distinguished. Well defined reflections of $CuFe_2O_4$ (a=8.39 Å, PDF 25-283) appear after 1 h of milling and a tendency of copper ferrite crystallization during the prolonging of milling procedure is observed. This assumption is well illustrated by the average particles size and microstrain degree, determined from the experimental XRD profiles by using the Williamson–Hall equation

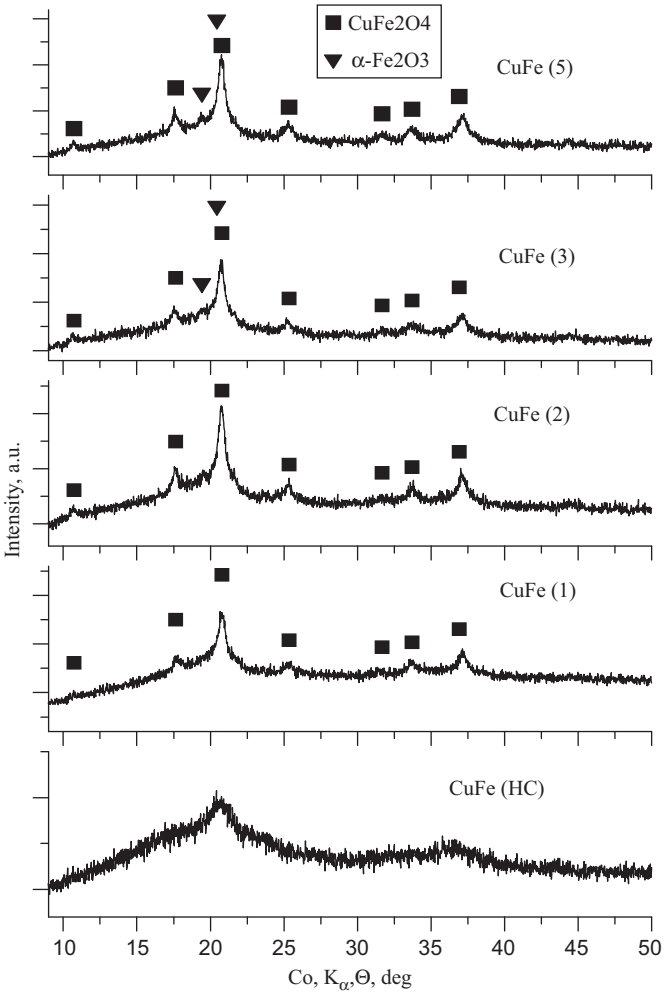

Fig. 1. XRD patterns of hydroxide carbonate precursor and the materials obtained after various milling duration.

Table 1
Average crystallites size (D), degree of microstrain (e) and lattice parameters (a) determined from the experimental XRD profiles.

Sample	Phase	D (nm)	$e \times 10^3$ (a.u.)	a (Å)
CuFe(1)	$CuFe_2O_4$-cubic	7.4	10.31	8.39
CuFe(2)	$CuFe_2O_4$-cubic	9.2	9.87	8.39
CuFe(3)	$CuFe_2O_4$-cubic	8.0	9.62	8.39
CuFe(5)	$CuFe_2O_4$-cubic	9.9	5.64	8.38

[30] (Table 1). The obtained data indicate the increase of ferrite crystal size in the range of 7–10 nm with about two fold decrease of microstrain degree with increasing of treatment duration from 1 to 5 h. We should stress on the formation of impurities of crystalline α-Fe_2O_3 phase (PDF 79-1741) in the case of the samples prepared after 3 and 5 h of milling.

In order to describe the state of iron containing phases more precisely, Mössbauer spectra of the studied materials were obtained (Fig. 2, Table 2). RT spectrum of CuFe(HC) sample exhibits a quadruple doublet with δ=0.36 mm/s, Δ=0.68 mm/s, indicating that the precursor is paramagnetic and the iron ions are in trivalent oxidized state. RT Mössbauer spectra of all materials after mechanochemical treatment represent doublets and sextets. The parameters of the doublet components of the spectra are typical of high spin Fe^{3+} ions in octahedral

coordination. It could be assigned to the presence of ultra dispersed iron containing particles with average size below 10–12 nm, which relative part slightly decreases with the increasing of milling time (Table 2). The higher values of Δ for these materials (0.86–0.93 mm/s) in comparison with that one for the precursor (0.68 mm/s) could be an indication for the changes in the environment of the Fe^{3+} ions after the milling procedure, probably due to the formation of new ferrite phase. The sextet component of the spectra is composed of two sextets with hyperfine field $B=48.2$ and 45.1 T and isomer shifting $\delta=0.37$ and 0.27 mm/s, respectively. They are generally assigned to Fe^{3+} ions in octahedral and tetrahedral coordination in copper ferrite, respectively ([12] and refs. therein). Their relative part increases after 5 h of milling time indicating higher degree of ferrite crystallization and agglomeration, which is in a good agreement with the XRD results (see above). New sextet component with relative weight $G=5\%$ and parameters corresponding to Fe^{3+} ions in hematite nanoparticles develops in the RT Mössbauer spectra of the samples obtained after 3 and 5 h of milling. Since the MS spectra of CuFe(1) and CuFe(2) do not contain lines typical of HC precursor, the observed hematite phase with longer mechanochemical treatment could be assigned to the partial decomposition of $CuFe_2O_4$. In order to distinguish the iron species, which represent doublet part of the RT Mössbauer spectra, LNT spectra were also recorded. An increase of the sextet components with parameters typical of hematite (11%) and copper ferrite (24–38%) is registered. In addition to the typical Mössbauer parameter changes with the temperature (increased values of δ and B) a preservation of the Δ value of hematite is observed. This can be explained by the small particle dimensions resulting in suppression of Morin's transition. So, hematite nanoparticles seem to be the main impurities of the obtained nanosized ferrite product, which particles size increases with the milling duration.

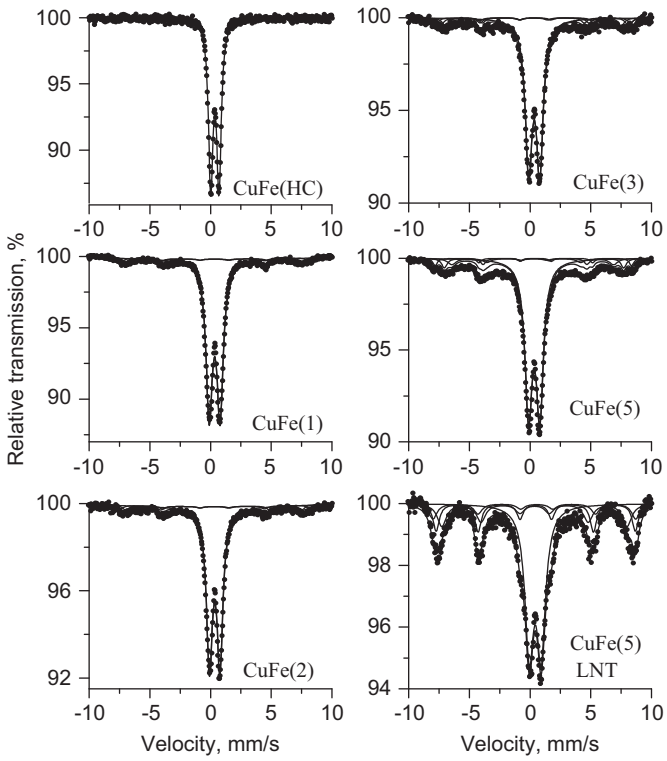

Fig. 2. RT Mössbauer spectra of hydroxide carbonate precursor and of mechanochemically synthesized samples; for comparison-LNT spectrum of CuFe(5).

The TPR profiles of all mechanochemically synthesized samples consist of two peaks (Fig. 3). The first sharp peak, appearing at 490–500 K, could be ascribed to the reductions of $CuFe_2O_4$ to metallic Cu and Fe_2O_3, and subsequent reduction of Fe_2O_3 to Fe_3O_4 [9,11,31]. The high-temperature peak with maximum at about 800 K is probably due to the reduction of Fe_3O_4 to Fe. The shift of the reduction effects towards the temperature axes for the various samples indicates some differences in their phase composition and particles size, as it was assumed also by XRD and Mössbauer study (Figs. 1 and 2, Tables 1 and 2).

Table 2
Parameters of Mössbauer spectra of the investigated samples.

Sample	Components	δ (mm/s)	Δ (mm/s)	B (T)	Γ_{exp} (mm/s)	G (%)
CuFe(HC)	Db-Fe^{3+}_{octa}	0.36	0.68	–	0.44	100
CuFe(1)	Sx1-$CuFe_2O_4$–Fe^{3+}_{octa}	0.37	0.00	48.2	0.60	5
	Sx2-$CuFe_2O_4$–Fe^{3+}_{tetra}	0.27	0.00	45.1	0.60	4
	Db-Fe^{3+}_{octa}	0.34	0.89	–	0.62	91
CuFe(2)	Sx1-$CuFe_2O_4$–Fe^{3+}_{octa}	0.37	0.00	48.2	0.60	5
	Sx2 -$CuFe_2O_4$–Fe^{3+}_{tetra}	0.27	0.00	45.1	0.60	6
	Db-Fe^{3+}_{octa}	0.34	0.86	–	0.57	89
CuFe(3) RT	Sx1-α-Fe_2O_3–Fe^{3+}_{octa}	0.37	−0.10	49.8	0.60	4
	Sx2-$CuFe_2O_4$–Fe^{3+}_{octa}	0.37	0.00	48.2	0.60	8
	Sx3-$CuFe_2O_4$–Fe^{3+}_{tetra}	0.27	0.00	45.1	0.60	8
	Db-Fe^{3+}_{octa}	0.34	0.91	–	0.66	80
CuFe(3) LNT	Sx1-α-Fe_2O_3–Fe^{3+}_{octa}	0.42	−0.10	51.3	0.80	11
	Sx2-$CuFe_2O_4$–Fe^{3+}_{octa}	0.47	0.05	51.2	0.62	12
	Sx3-$CuFe_2O_4$–Fe^{3+}_{tetra}	0.37	−0.02	47.6	0.87	12
	Db-Fe^{3+}_{octa}	0.43	0.92	–	0.68	65
CuFe(5) RT	Sx1-α-Fe_2O_3–Fe^{3+}_{octa}	0.37	−0.10	50.3	0.43	5
	Sx2-$CuFe_2O_4$–Fe^{3+}_{octa}	0.37	−0.04	45.9	0.54	9
	Sx3-$CuFe_2O_4$–Fe^{3+}_{tetra}	0.27	−0.05	44.1	0.82	10
	Db-Fe^{3+}_{octa}	0.34	0.93	–	0.71	76
CuFe(5) LNT	Sx1-α-Fe_2O_3–Fe^{3+}_{octa}	0.45	−0.10	51.9	0.80	11
	Sx2-$CuFe_2O_4$–Fe^{3+}_{octa}	0.47	0.00	51.0	0.62	19
	Sx3-$CuFe_2O_4$–Fe^{3+}_{tetra}	0.37	0.00	47.4	0.90	19
	Db-Fe^{3+}_{octa}	0.43	0.98	–	0.85	51

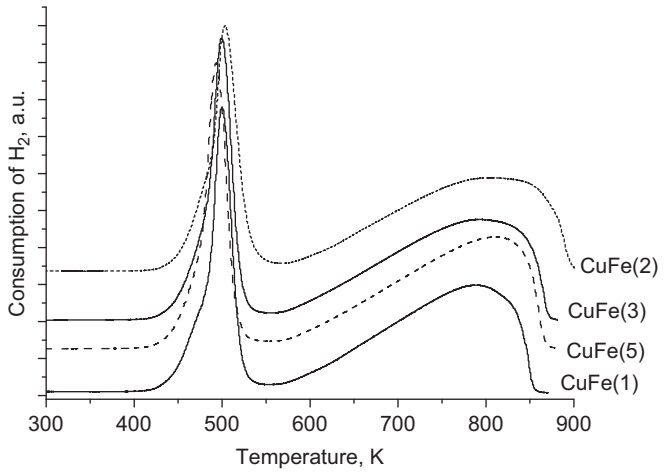

Fig. 3. TPR profiles of mechanochemically synthesized materials.

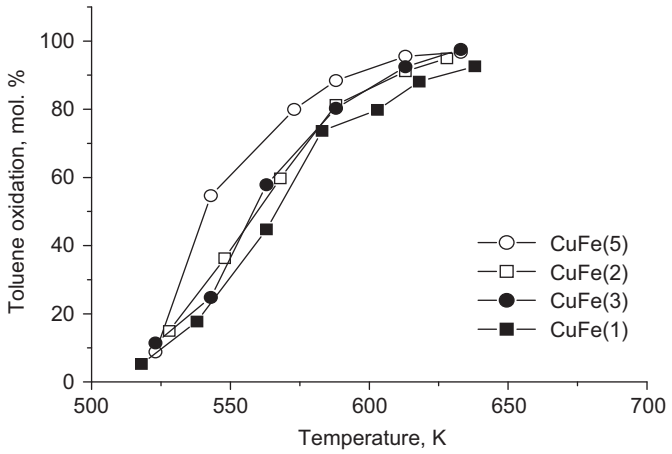

Fig. 4. Temperature dependencies of toluene total oxidation for various mechanochemically synthesized materials.

3.2. Catalytic study

The temperature dependencies of total oxidation of toluene for various samples are presented in Fig. 4. For all materials the conversion started above 520 K and about 100% combustion of toluene to CO_2 was achieved at about 620–630 K. We should stress on the similarity of the catalytic behavior of the samples, obtained under different milling time, despite the differences observed in their initial phase composition (see above). The sample CuFe(5) exhibits the best catalytic activity, which well correlates with its reduction ability (Fig. 3). This result is not surprising in a view of the data reported in the literature [32], where Mars van Krevelen mechanism, including the release of oxygen from the catalyst lattice, is generally discussed. The RT Mössbauer spectra of the samples after the catalytic test (Table 3, Fig.6) represent sextets of copper ferrite and about 30% α-Fe_2O_3 is observed. This phase composition as well as the formation of small amount of CuO nanoparticles is confirmed by the XRD patterns of the used materials (Fig. 7). Comparing the phase composition of the samples before and after the catalytic test (Tables 2 and 3; Figs. 2 and 6), the intensive crystallization and agglomeration of the spinel ferrite particles under the oxidative reaction medium is assumed. Moreover, the changes in the relative part of both sextet components in the Mössbauer spectra after the catalytic test reveal an increase in the inversion parameter of the spinel lattice, which corresponds to higher

Table 3
Parameters of Mössbauer spectra of the investigated samples after the catalytic test: *t*-total oxidation of toluene; M-methanol decomposition.

Sample	Components	δ (mm/s)	Δ (mm/s)	B (T)	Γ_{exp} (mm/s)	G (%)
CuFe(3)_t	Sx1-α-Fe_2O_3–Fe^{3+}_{octa}	0.38	−0.10	51.3	0.35	28
	Sx2-$CuFe_2O_4$–Fe^{3+}_{octa}	0.30	−0.04	48.4	0.62	27
	Sx3-$CuFe_2O_4$–Fe^{3+}_{tetra}	0.22	−0.01	45.4	0.93	38
	Db-Fe^{3+}_{octa}	0.30	0.82	–	0.62	7
CuFe(5)_t	Sx1-α-Fe_2O_3–Fe^{3+}_{octa}	0.38	−0.10	51.8	0.35	30
	Sx2-$CuFe_2O_4$–Fe^{3+}_{octa}	0.32	−0.04	48.5	0.64	31
	Sx3-$CuFe_2O_4$–Fe^{3+}_{tetra}	0.23	0.00	45.3	1.02	39
CuFe(1)_M	Sx1-Fe_3O_4–Fe^{3+}_{tetra}	0.29	0.00	48.2	0.31	1
	Sx2-Fe_3O_4–$Fe^{2,5+}_{octa}$	0.69	0.00	44.7	0.36	2
	Sx3-χ-Fe_5C_2	0.24	0.05	22.1	0.45	35
	Sx4-χ-Fe_5C_2	0.22	0.01	19.1	0.43	36
	Sx5-χ-Fe_5C_2	0.19	0.01	11.4	0.52	26
CuFe(2)_M	Sx1-χ-Fe_5C_2	0.26	0.05	22.0	0.45	37
	Sx2-χ-Fe_5C_2	0.22	0.01	18.9	0.52	37
	Sx3-χ-Fe_5C_2	0.18	0.01	11.2	0.49	26
CuFe(3)_M	Sx1-Fe_3O_4–Fe^{3+}_{tetra}	0.29	0.00	48.2	0.50	1
	Sx2-Fe_3O_4–$Fe^{2,5+}_{octa}$	0.65	0.00	44.8	0.60	2
	Sx3-χ-Fe_5C_2	0.26	0.04	22.2	0.41	31
	Sx4-χ-Fe_5C_2	0.21	0.01	18.9	0.46	39
	Sx5-χ-Fe_5C_2	0.19	0.01	11.3	0.50	27
CuFe(5)_M	Sx1-Fe_3O_4–Fe^{3+}_{tetra}	0.27	0.00	48.2	0.50	2
	Sx2-Fe_3O_4–$Fe^{2,5+}_{octa}$	0.66	0.00	45.1	0.50	3
	Sx3-χ-Fe_5C_2	0.27	0.04	22.4	0.44	32
	Sx4-χ-Fe_5C_2	0.21	0.01	19.0	0.53	38
	Sx5-χ-Fe_5C_2	0.19	0.01	11.7	0.50	25

occupation of the octahedral positions by Cu^{2+} ions. According to [1,13–19], the increase of the population of the Cu^{2+} cations in the B-sublattice provides the cooperative Jan-Teller distortion and transformation of crystal phase to tetragonal one. This transformation is well illustrated by the XRD patterns of the samples after the catalytic test, where both cubic and tetragonal ferrite phase are registered (Fig. 7). According to [33], the increasing amount of the octahedrally coordinated copper ions in the spinel structure, which is observed after the catalytic test, could also facilitate the catalytic process, due to the fact that the catalytic properties of the spinel materials are mainly determined by the more exposed to the surface octahedrally coordinated cations. So, the increase in the reduction ability and the catalytic activity in toluene oxidation is considered as a result of higher degree of crystallization of a mixture of hematite, CuO and ferrite phase.

In Fig. 5 the temperature dependencies of methanol decomposition on various materials are compared. On the contrary to the catalytic behavior of the samples in the oxidative reaction atmosphere, which exists during the toluene oxidation (Fig. 4), here a complex conversion curves with a maximum at about 550 K and further conversion increase above 600 K, are observed. The selectivity to CO is about 75–80% in a whole investigated temperature interval with the formation of methane, CO_2 and dimethyl ether as by-products. The best catalytic activity is registered for CuFe(5), which well corresponds with its high reduction ability (Fig. 3). However the order of the catalytic activity of the other samples does not follow their arrangement in the reduction ability. After the catalytic test, RT Mössbauer spectra of all materials (Fig. 6, Table 3) represent three sextets with hyperfine field of about 22, 19 and 11 T, which are assigned to the formation of new iron carbide (χ-Fe_5C_2) phase [34]. With the exception of the CuFe(2), the spectra of the other materials consists of two additional sextets with parameters, corresponding to Fe_3O_4 phase with relative part about 3–5%. These transformations of the initial iron containing phase are also confirmed by the XRD patterns of the samples after the catalytic test (Fig. 7), where

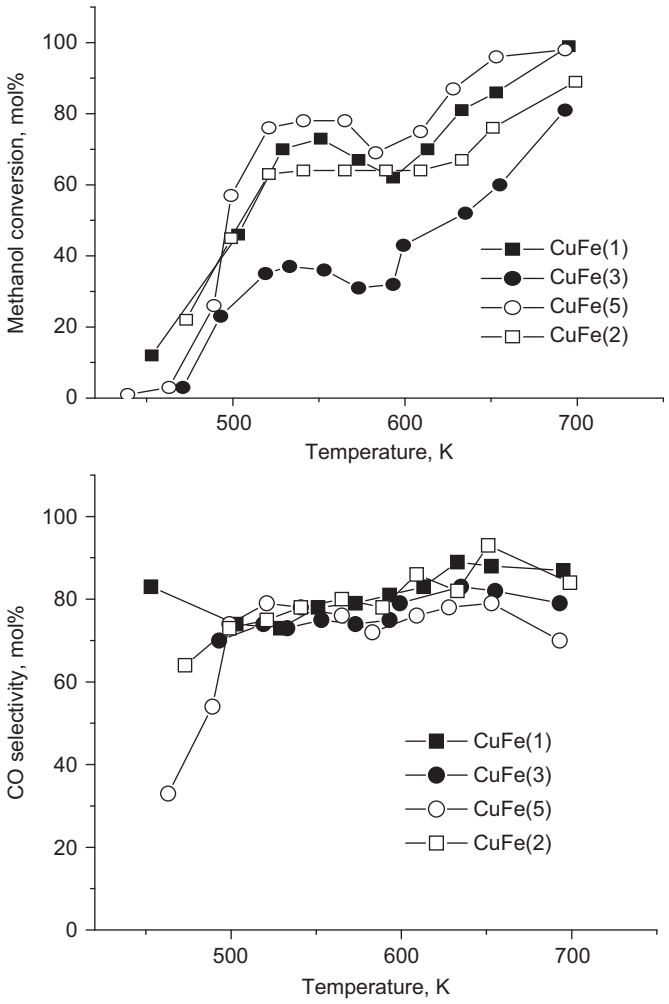

Fig. 5. Temperature dependencies of conversion and CO selectivity in methanol decomposition for various mechanochemically synthesized materials.

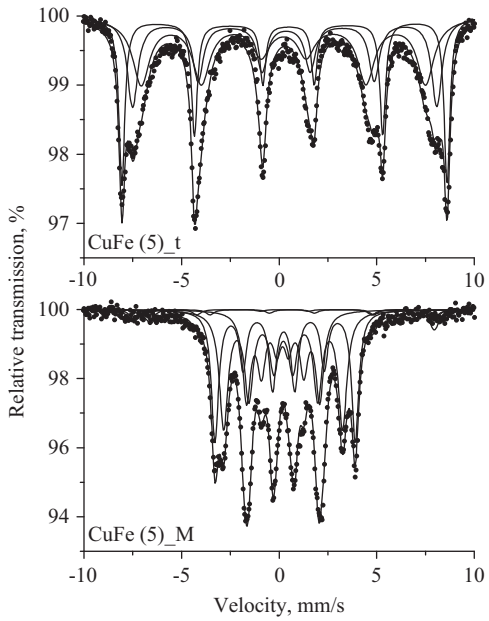

Fig. 6. Typical RT Mössbauer spectra of CuFe(5) sample after methanol decomposition (CuFe(5)_M) and total oxidation of toluene (CuFe(5)_t).

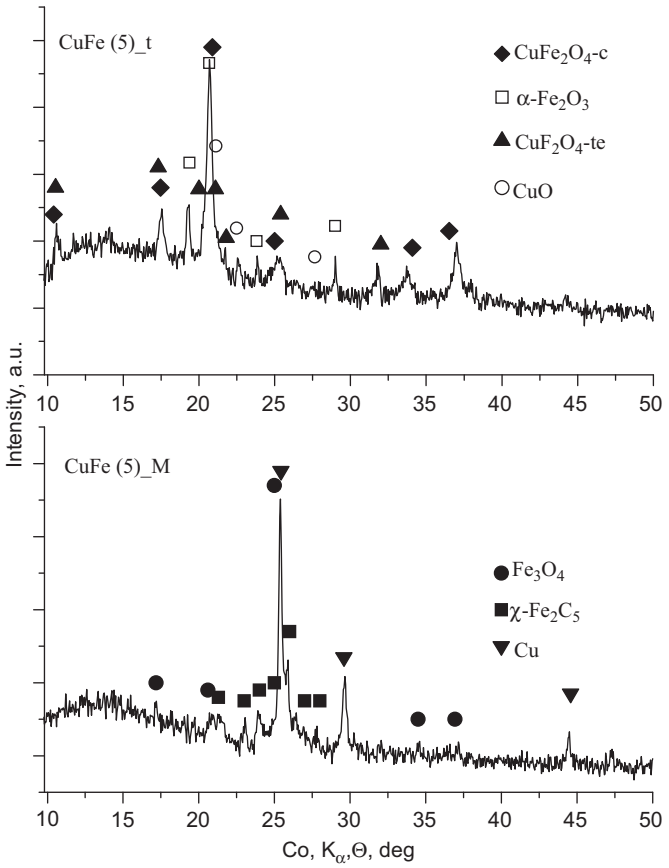

Fig. 7. XRD patterns of CuFe(5) sample after total oxidation of toluene (CuFe(5)_t) and methanol decomposition (CuFe(5)_M).

magnetite, iron carbide and metallic copper are registered. So, the intensive processes of reduction and decomposition of the initial ferrite phase occur by the influence of the reduction reaction medium. Obviously, these phase transformations under the reduction medium provides the observed complex catalytic behavior of the studied ferrites with the temperature increase and it is determined by the current ratio between the various iron- and copper-containing active components, such as metallic copper, ferrite, hematite, magnetite and iron carbide [35].

4. Conclusions

The co-precipitation of copper and iron hydroxide carbonates and their high-energy ball milling, facilitates the formation of nanocrystalline copper ferrites with cubic crystal structure. The phase composition of the obtained materials depends on the milling duration. The catalytic properties of ferrites are strongly influenced by their phase transformations under the reaction medium. Predominantly agglomeration and further crystallization of spinel ferrite nanoparticles occurs under the oxidation reaction medium during the toluene oxidation. Almost total transformation of ferrite phase to metallic copper, magnetite and iron carbide is observed under the reduction reaction medium, which realizes during the methanol decomposition and facilitates the selective formation of hydrogen and CO.

Acknowledgments

Financial support of the National Science Fund of the Bulgarian Ministry of Education and Science through projects

DO 02-295/2008, Rila 4-412 (DO 02-29/2008) and TK 02-63 is acknowledged.

References

[1] S.J. Stewart, M.J. Tueros, G. Cernicchiaro, R.B. Scorzelli, Solid State Commun. 129 (2004) 347–351.
[2] H. Ehrhard, S. Campbell, M. Hofmann, J. Alloys Compd. 339 (2002) 255–260.
[3] W. Ponhan, S. Maensiri, Solid State Sci. 11 (2009) 479–484.
[4] L. Satyaranaya, K.M. Reddy, S.V. Manorama, Sensors Actuators B 89 (2003) 62–67.
[5] K.S. Kang, C.H. Kim, W.C. Cho, K.K. Bae, S.W. Woo, C.S. Park, Int. J. Hydrogen Energy 33 (2008) 4560–4568.
[6] H. Yang, J. Yan, Z. Lu, X. Cheng, Y. Tang, J. Alloys Compd. 476 (2009) 715–719.
[7] H.G. El-Shobaky, Y.M. Fahmy, Mater Res. Bull. 41 (2006) 1701–1713.
[8] G.R. Dube, V.S. Darshane, J. Mol. Catal. 79 (1993) 285–296.
[9] K. Faungnawakij, Y. Tanaka, N. Shimoda, T. Fukunaga, R. Kikuchi, K. Eguchi, Appl. Catal. B: Environ. 74 (2007) 144–151.
[10] K. Eguchi, N. Shimoda, K. Faungnawakij, T. Matsui, R. Kikuchi, S. Kawashima, N. Sugiyama, K. Kurushima, Appl. Catal. B: Environ. 80 (2008) 156–167.
[11] K. Faungnawakij, R. Kikuchi, T. Fukunaga, K. Eguchi, Catal. Today 138 (2008) 157–161.
[12] J.Z. Jiang, G.F. Goya, H.R. Rechenberg, J. Phys.: Condens. Matter 11 (1999) 4063–4078.
[13] G.F Goya, H.R. Rechenberg, J. Appl. Phys. 84 (1998) 1101–1108.
[14] M. Estrella, L. Barrio, G. Zhou, X. Wang, Q. Wang, W. Wen, J.C. Hanson, A.I. Frenkel, J.A. Rodriguez, J. Phys. Chem. C 113 (2009) 14411–14417.
[15] K.J. Kima, J.H. Lee, S.H. Lee, J. Magn. Magn. Mater. 279 (2004) 173–177.
[16] A. Dias, R.L. Moreira, Mater. Lett. 39 (1999) 69–76.
[17] R.A. McCurrie, In: Ferromagnetic Materials: Structure and Properties, Academic Press, London, 1994.
[18] M. Yokoyama, A. Nakamura, T. Sato, K. Haneda, J. Magn. Soc. Jpn. 22 (1998) 243–245.
[19] I. Nedkov, R.E. Vandenberghe, T. Marinova, P. Thailhades, T. Merodiiska, I. Avramova, Appl. Surf. Sci. 253 (2006) 2589–2596.
[20] R.H. Kodama, A.E. Berkowitz, E.J. McNiff, S. Foner, Phys. Rev. Lett. 77 (1996) 394–397.
[21] L. Suber, R. Zysler, A.G. Santiago, D. Fiorani, M. Angiolini, A. Montone, J.L. Dormann, Mater. Sci. Forum 937 (1998) 269–272.
[22] J.M.D. Coey, Phys. Rev. Lett. 27 (1971) 1140–1142.
[23] P.B. Pandya, H.H. Joshi, R.G. Kulkarni, J. Mater. Sci. Lett. 10 (1991) 474–476.
[24] Z. Sun, L. Liu, D. Jia, W. Pan, Sensor Actuators B: Chem. 125 (2007) 144–148.
[25] S.W. Tao, F. Gao, X.Q. Liu, O.T. Sørensen, Mater. Sci. Eng. B 77 (2007) 172–176.
[26] C. Despax, P. Tailhades, C. Baubet, C. Villette, A. Rousset, Thin Solid Films 293 (1997) 22–28.
[27] S. Roy, J. Ghose, J. Magn. Magn. Mater. 307 (2006) 32–37.
[28] R.K. Selvan, C.O. Augusin, L.J. Berchmans, R. Saraswathi, Mater. Res. Bull. 38 (2003) 41–54.
[29] E. Manova, D. Paneva, B. Kunev, C. Estournès, E. Rivière, K. Tenchev, A. Léaustic, I. Mitov, J. Alloys Comp. 485 (2009) 356–361.
[30] E. Manova, C. Estournès, D. Paneva, J.L. Rehspringer, T. Tsoncheva, B. Kunev, I. Mitov, Hyperfine Interact. 165 (2005) 215–220.
[31] S. Kameoka, T. Tanabe, A.P. Tsai, Catal. Lett. 100 (2005) 89–93.
[32] L.C.A. Oliveira, R.M. Lago, J.D. Fabris, K. Sapag, Appl. Clay Sci. 39 (2007) 218–222.
[33] H.G. El-Shobaky, M.M. Mokhtar, Appl. Surf. Sci. 253 (2007) 9407–9413.
[34] G.P. Raupp, W.N. Delgass, J. Catal. 58 (1979) 348–360.
[35] T. Tsoncheva, J. Rosenholm, C.V. Teixeira, M. Dimitrov, M. Linden, C. Minchev, Microporous Mesoporous Mater. 89 (2006) 209–218.